CrossMark

The Impact of Stellar Rotations and Binaries on the Shape of Upper Main Sequence near Turnoff in Open Cluster NGC 6067

Jayanand Maurya[1] , Yu Zhang[1,2] , Sebastian Kamann[3] , Hubiao Niu[1] , Yves Frémat[4] , Kaixiang Lang[1] , Y. C. Joshi[5] ,
M. R. Samal[6] , Peter De Cat[4] , and Ali Esamdin[1,2]

[1] Xinjiang Astronomical Observatory, Chinese Academy of Sciences, No. 150, Science 1 Street, Urumqi, Xinjiang 830011, People's Republic of China; maurya.jayanand@gmail.com, zhy@xao.ac.cn

[2] School of Astronomy and Space Science, University of Chinese Academy of Sciences, Beijing 100049, People's Republic of China

[3] Astrophysics Research Institute, Liverpool John Moores University, IC 2 Liverpool Science Park, 146 Brownlow Hill, Liverpool L3 5RF, UK

[4] Royal Observatory of Belgium, Avenue circulaire 3, 1180 Bruxelles, Belgium

[5] Aryabhatta Research Institute of Observational Sciences (ARIES), Manora Peak, Nainital 263002, India

[6] Astronomy & Astrophysics Division, Physical Research Laboratory, Ahmedabad 380009, India

Abstract

We present the analysis of the extended main-sequence turnoff (eMSTO) in the open cluster NGC 6067. We derive the projected rotational velocity, $v\sin i$, of the stars belonging to the eMSTO region of the main sequence (MS) utilizing Gaia-ESO spectra. Our results reveal a positive correlation between $v\sin i$ and the color of eMSTO stars, where fast-rotating stars predominantly occupy the red part of the MS while slow-rotating ones prefer a bluer side of the MS. The gravity-darkening effect might be a reason for this correlation. We find that most of the close binaries present in the eMSTO population would be slow-rotating due to the tidal-locking phenomenon. We identify four double-lined spectroscopic binaries (SB2) featuring slow-rotating companions, further supporting this tidal-locking hypothesis. However, the spatial distribution and the cumulative radial distribution indicate a higher concentration of red eMSTO stars in the cluster's central region than their bluer counterparts. This suggests that tidal locking is less likely to be the cause of the observed spread in rotation rates among eMSTO stars. Instead, we propose that star–disk interactions during the pre-main-sequence phase might have played a crucial role in spreading the rotation rates of stars, leading to the eMSTO phenomenon in NGC 6067.

Unified Astronomy Thesaurus concepts: Open star clusters (1160); Stellar rotation (1629); Blue straggler stars (168); Close binary stars (254); Spectroscopy (1558)

1. Introduction

The presence of the extended main-sequence turnoff (eMSTO) in open clusters has attracted scientific curiosity about the stellar composition of the clusters. The extended star formation over a period of 100–500 Myr has been initially attributed to the origin of the eMSTO in star clusters (A. P. Milone et al. 2009; P. Goudfrooij et al. 2014). The second-generation stars born out of extended star formation are expected to be less populous than the first-generation stars, which does not hold true in observations (K. Bekki & A. D. Mackey 2009). Additionally, there has not been any detection of the extended star formation on a scale of a few hundred million years (I. Cabrera-Ziri et al. 2016). Considering the shortcomings of the models proposed for the extended star formation, N. Bastian & S. E. de Mink (2009) proposed that the spread in rotation velocity of the stars in the upper MS can mimic the eMSTO in star clusters. The reduced gravity near the equator of stars due to rotation manifests into lower effective temperatures and luminosities for fast-rotating stars (H. von Zeipel 1924). This gravity-darkening effect, combined with the viewing angle for the stars, may lead to a spread in color in the upper MS and, hence, can cause the eMSTO in the clusters (J. Maurya et al. 2024). Additionally, the rotational mixing in the stars can modify the chemical composition of the

stellar envelope and enhance the stellar core size, which results in lower temperatures and higher luminosities for the fast-rotating stars (A. Palacios et al. 2003). Many previous studies also find observational evidence that the color of the eMSTO stars in the color–magnitude diagram (CMD) is correlated with their rotational velocity (N. Bastian et al. 2018; S. Kamann et al. 2020; W. Sun et al. 2021).

All the MS stars with masses below $\sim 1.6\,M_\odot$ are expected to be slow-rotating because of the magnetic braking of their rotations (R. P. Kraft 1967). So, if the eMSTO in the open clusters is to be caused by the spread in rotation velocity, then the group of the eMSTO stars should be heavier than $\sim 1.6\,M_\odot$ to also comprise fast-rotating stars. This scenario for the lower mass limit of the eMSTO stars is also found to be true in some previous studies (N. Bastian et al. 2020; S. Kamann et al. 2020). However, the lower mass limit is predicted to depend on the open clusters' metallicity (C. Georgy et al. 2019). Older clusters cannot host massive stars, so the lower mass limit indicates a certain age limit for the open clusters to host the eMSTO. Only clusters below 2 Gyr of age are predicted to host the eMSTO in the Large Magellanic Cloud (C. Georgy et al. 2019). The open clusters below 2 Gyr ages are found to host the eMSTO in the Milky Way (G. Cordoni et al. 2023). However, the age limit at which the eMSTO disappears shifts toward older age with increasing metallicity (C. Georgy et al. 2019).

The possible mechanisms that may produce the observed spread in rotational velocity of the eMSTO stars having similar masses are also interesting to explore. Interacting binaries may

play a role in producing the spread in the rotational velocity of the eMSTO stars. F. D'Antona et al. (2015) suggested that tidal interactions in binary stars cause the initially fast-rotating stars to slow down and thus produce the spread in the rotational velocity of the stars. In such a scenario, tidally locked binaries would populate the blue part of the eMSTO and are expected to be preferentially located in the central region of the cluster. However, J. Maurya et al. (2024) found that the stars in the blue part of the eMSTO were preferentially located in the outer region of the cluster NGC 2355. Similar spatial distribution patterns for the blue and the red parts of the eMSTO populations were also reported in previous studies (S. Kamann et al. 2023; F. Niederhofer et al. 2024). If tidal interactions in binaries were the main rotation braking mechanism, blue eMSTO stars should exhibit a higher binary fraction than red eMSTO stars. This is because blue eMSTO stars tend to rotate more slowly, which aligns with the idea that binary interactions slow down stellar rotation. However, similar binary fractions have been found across the eMSTO region in the CMD for a few instances, which appear to be at odds with the proposed binary interaction mechanism for the origin of the spread in rotational velocity of the eMSTO stars (S. Kamann et al. 2020, 2021).

An alternative model to the interacting binary model explaining the spread in rotational velocity of the eMSTO in star clusters is proposed by N. Bastian et al. (2020). In this model, the observed spread in the rotational velocity of the eMSTO stars is attributed to the spread in the rotational velocity distribution of the stars during their pre-main-sequence (PMS) phase due to star–disk interaction (SDI) phenomena. The stars lose angular momentum due to the coupling of their circumstellar disk. The stars that lose their circumstellar disk early become free to spin up due to the star's contraction to the MS. Thus, the stars retaining their circumstellar disk for a longer period rotate slowly compared to the stars losing the disk earlier. The spread in rotation velocity during the PMS phase persists up to the age of ∼1.5 Gyr for stars on the MS. The SDI causing the spread in rotation rates of the stars is suggested to be the reason for the origin of the eMSTO in open cluster NGC 2355 (J. Maurya et al. 2024).

C. Wang et al. (2022) suggest that the binary mergers may produce slow-rotating blue eMSTO stars in star clusters. According to this theory, a binary merger will rejuvenate the stellar core with more hydrogen fuel, which causes the star to appear bluer than coeval single stars of the same mass. The merger product star rotates slowly due to the loss of angular momentum during the thermal expansion phase post-coalescence and internal restructuring.

The eMSTO in star clusters has been mostly attributed to the spread in rotational velocity of the stars. However, other mechanisms have also been suggested to contribute to the origin of the eMSTO in the star clusters. The dust-like extinction from an excretion disk of the fast-rotating star can cause the star to appear redder than its nonrotating counterparts, which may produce the eMSTO (F. D'Antona et al. 2023). The differential reddening across the clusters may also resemble the eMSTO (J. Alonso-Santiago et al. 2021). Similarly, binary stars with different mass ratios can create a redder spread in color on the MS compared to the single stars resembling the eMSTO (J. Chen et al. 2022).

In this paper, we present the study of the eMSTO in the open cluster NGC 6067. This cluster is known to host Be stars and SB2s, which are interesting objects to understand the role of stellar rotation and tidally interacting binaries in the origin of the eMSTO in open clusters (J. Alonso-Santiago et al. 2017). NGC 6067, aged 126 Myr, is among the relatively young open clusters for hosting the eMSTO (T. Cantat-Gaudin et al. 2020). J. Alonso-Santiago et al. (2017) estimated the mean radial velocity of the cluster to be -39.5 ± 0.9 km s^{-1} using high-resolution ($R = 48,000$) spectra of 45 member stars.

2. Data

2.1. Photometric

We utilized Gaia Data Release 3 (DR3) astrometric and photometric data to identify member stars and further analyze the cluster NGC 6067 (Gaia Collaboration et al. 2016, 2023). Gaia-DR3 astrometric data is especially useful for the study of the eMSTO phenomenon as it provides a very high accuracy of ∼0.03 mas yr^{-1} in the proper motions and a similar accuracy of ∼0.03 mas in parallax for bright stars with $G < 15$ mag (Gaia Collaboration et al. 2023). The astrometric data from Gaia-DR3 has median uncertainties of 0.07 and 0.5 mas yr^{-1} in proper motions and 0.07 and 0.5 mas in parallax for stars up to $G = 17$ and $G = 20$ mag, respectively. The Gaia-DR3 provides good accuracy for the photometric data, too. It has uncertainties of 0.001, 0.012, and 0.006 mag in the G, G_{BP}, and G_{RP} bands for bright stars up to 17 mag. Gaia-DR3 has relatively high photometric uncertainties of 0.006, 0.108, and 0.052 mag for stars with $G = 20$ mag.

2.2. Spectroscopic

We used the spectroscopic data from the European Southern Observatory (ESO) archives observed under program IDs 188. B-3002(M) and 095.C-0818(A). The spectra were observed from the Ultraviolet and Visual Echelle Spectrograph (UVES) and GIRAFFE spectrographs mounted on the ESO Very Large Telescope. The spectral resolutions ($\frac{\lambda}{\Delta\lambda}$) for UVES and GIRAFFE are ∼51,000 and 29,000, respectively. These spectra typically have a signal-to-noise ratio above ∼50. The spectra from UVES have a wavelength range from 420 to 620 nm. The spectra from GIRAFFE are in the wavelength ranges 385–405 nm and 515–535 nm. In the Gaia-ESO archives, we found spectra for 41 stars, including four SB2 and two Be stars, belonging to the upper MS of NGC 6067. Seven of these 41 stars have high-resolution UVES spectra; the remaining have GIRAFFE spectra. We also utilized Gaia-ESO spectra for two blue straggler stars (BSS) and 14 red giant branch stars (RGB) to estimate their rotational and radial velocities. Only one of the two BSS stars has UVES spectra. All the spectra of giant stars were taken with the UVES spectrograph. In general, only one or two spectra are available in the Gaia-ESO archives for each of these upper MS, BSS, and RGB stars.

3. Physical Properties

3.1. Membership and Physical Parameters

We identified the member stars of NGC 6067 using the Hierarchical Density-Based Spatial Clustering of Applications with Noise (HDBSCAN) algorithm (L. McInnes et al. 2017). We used Gaia-DR3 proper motions and parallaxes to identify
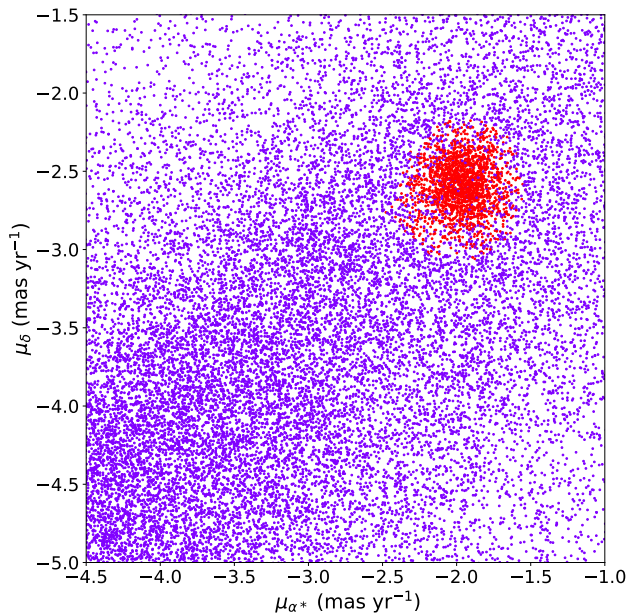
Figure 1. The cluster overdensity in the proper motions space. The red points represent potential cluster member stars. Blue points denote the field stars.

Table 1
Physical Parameters of NGC 6067 Obtained in the Present Study

log (age) (yr)	Mean Parallax (mas)	Distance (pc)	[Fe/H] (dex)
7.96 (1)	0.472 ± 0.045 (1)	1960 ± 89 (1)	−0.11 ± 0.02 (1)
8.10 (2)	0.471 ± 0.038 (3)	1957 (3)	+0.03 ± 0.27 (4)
…	…	…	+0.19 ± 0.05 (5)

Note. We have also provided values of these parameters from the literature for comparison. References: (1) present study; (2) T. Cantat-Gaudin et al. (2020); (3) E. L. Hunt & S. Reffert (2023); (4) A. E. Ray et al. (2022); (5) J. Alonso-Santiago et al. (2017).

clustering and obtain the membership probability of stars (Gaia Collaboration et al. 2016, 2023). We used proper motions ($\mu_{\alpha*}$, μ_δ) and parallax (ϖ) as input parameters for the overdensity identification through the HDBSCAN. To avoid the inclusion of bad data points, we included only those stars with parallax uncertainty below 0.25 mas in our sample for overdensity identification. We chose minimum cluster size, minimum samples, and maximum cluster size to be 400, 400, and 1800 for overdensity detection. The resulting overdensity is shown in Figure 1. Stars having a membership probability greater than 70% were considered as member stars. We then plotted the cluster's CMD and removed nine outlier stars, which were found to be significantly deviating from the MS in visual inspection of the CMD. These stars have G magnitude greater than 14.6 mag. Four out of the nine outliers are fainter than 18 mag in the G band. Finally, we obtained 944 member stars in the cluster NGC 6067. Out of the 944 member stars identified by us, 867 and 633 are common with those listed by E. L. Hunt & S. Reffert (2023) and T. Cantat-Gaudin et al. (2020), respectively. Gaia-DR3 offers proper motions and parallaxes for 10% more sources than Gaia-DR2, with significantly improved precision (C. Fabricius et al. 2021; L. Lindegren et al. 2021). The increased number of sources with astrometric solutions and better precision likely accounts for the smaller overlap of member stars with the T. Cantat-Gaudin et al. (2020) catalog, which is based on Gaia-DR2 data. Additionally, T. Cantat-Gaudin et al. (2020) includes stars only up to $G = 17.8$ mag for NGC 6067, while our sample extends to $G = 18.6$ mag, which may also explain the lower number of common members.

The mean parallax of the member stars is calculated to be 0.472 ± 0.045 mas, which corresponds to a distance of 1960 ± 89 pc after applying the global systematic offset of -0.039 mas in the parallax (M. A. T. Groenewegen 2021). The mean parallax and distance obtained agree well with their values as 0.471 ± 0.038 mas and 1957 pc provided by E. L. Hunt & S. Reffert (2023). We fitted an extinction-corrected isochrone to the CMD constructed from the

identified member stars to estimate the cluster's age. We took the extinction value to be $A_V = 0.99$ mag as provided by E. L. Hunt & S. Reffert (2023). The best fit was obtained for an isochrone corresponding to a log(age) of 7.96 yr, which corresponds to a cluster age of 91 Myr. We used metallicity $Z = 0.02$ for the isochrones, which was calculated from the [Fe/H] abundance of -0.11 ± 0.02 dex as estimated in Section 4. The physical parameters of NGC 6067 are summarized in Table 1. The extinction-corrected P. Marigo et al. (2017) isochrone fitted on the CMD of NGC 6067 is shown in Figure 2. As clearly visible in the figure, we detected a broadened upper MS resembling an eMSTO. We considered the MS stars having G band magnitudes from 9.85 to 14.05 mag and $G_{BP} - G_{RP}$ color between 0.20 and 0.70 mag to be the eMSTO stars. This way, we found 280 eMSTO stars in the CMD of NGC 6067, as shown by the black points in Figure 2. The masses of the eMSTO stars are estimated to be in the range of 2.1–5.3 $M_\odot$ through isochrone fitting on the CMD of the cluster. The MS stars fainter than the eMSTO stars and lying in the lower MS are termed as lMS stars.

3.2. Differential Reddening

The differential reddening in an open cluster region may also contribute to the $G_{BP} - G_{RP}$ color spread in the upper MS of the cluster. We utilized the line-of-sight extinction, A_V, in the V band provided by A. Khalatyan et al. (2024) to investigate the extinction across NGC 6067. A. Khalatyan et al. (2024) estimated A_V values with a median uncertainty of 0.20 mag through the gradient-boosted random-forest regressor (xgboost) algorithm using Gaia-DR3 multiband photometry, astrometry, and most notably XP spectra. We have shown the 2D reddening, $E(B - V)$, map of the eMSTO stars of NGC 6067 in Figure 3. We calculated the $E(B - V)$ from A_V values using the relation $E(B - V) = A_V/3.1$, based on the extinction law with $R_V = 3.1$ (J. A. Cardelli et al. 1989). The 2D reddening map for the eMSTO stars is shown in Figure 3. The reddening map reveals a mild differential reddening with $E(B - V)$ varying from 0.23 to 0.40 mag for the eMSTO stars across the NGC 6067 cluster, considering the inherent median uncertainty of 0.20 mag in A_V values taken from A. Khalatyan et al. (2024). D. G. Turner (2016) reported similar color excesses but slightly shifted toward higher values for NGC 6067, ranging from $E(B - V) = 0.30$ to 0.48 mag.

To correct for differential reddening, we followed the method outlined by A. P. Milone et al. (2012) and generated a differential reddening-corrected MS for NGC 6067. Here, we briefly outline the procedure. We initially arbitrarily chose a point (O) near MS turnoff in the CMD as shown by the red
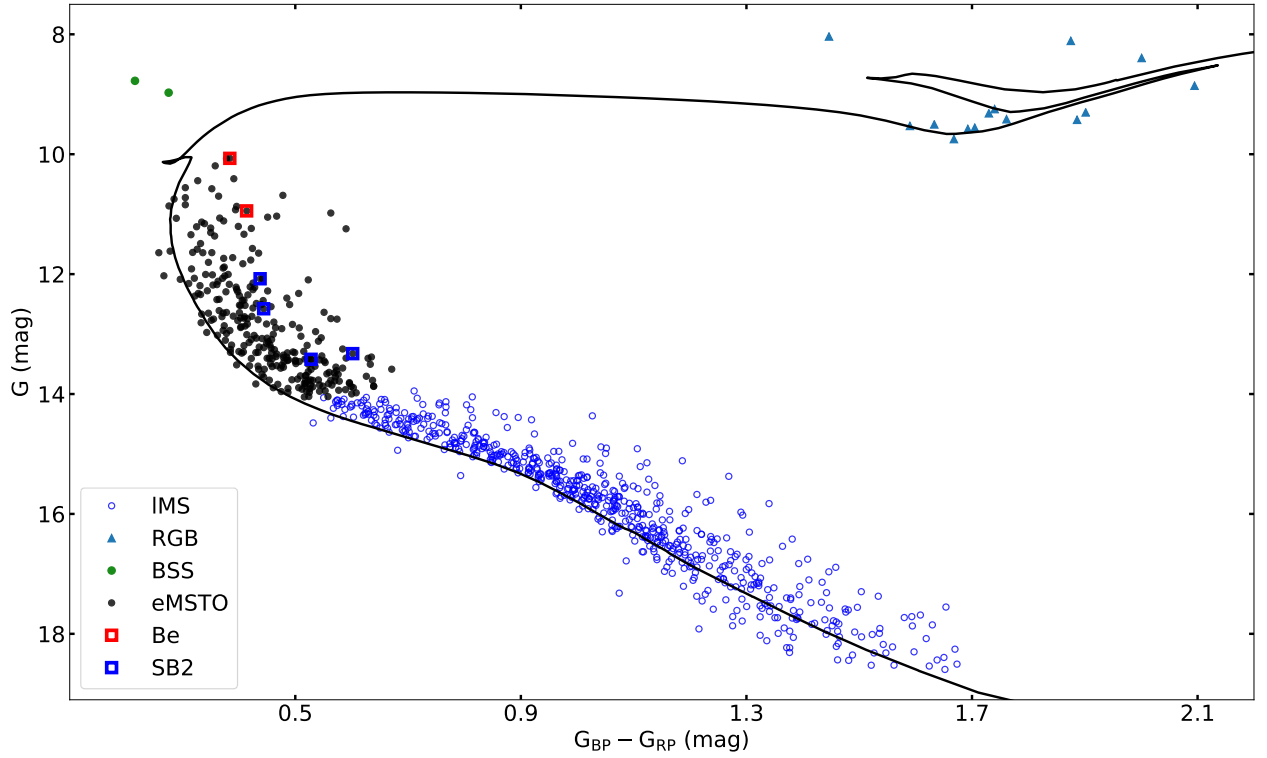
Figure 2. The color–magnitude diagram of the cluster NGC 6067. The stars belonging to the eMSTO are shown by black points. The eMSTO stars also include Be stars enclosed by red squares and SB2 stars enclosed by blue squares. The RGB, BSS, and lMS stars are also shown by the markers given in the legend of the figure. The black continuous curve shows the best-fit (P. Marigo et al. 2017) isochrone corresponding to the logarithmic age of 7.96 yr.
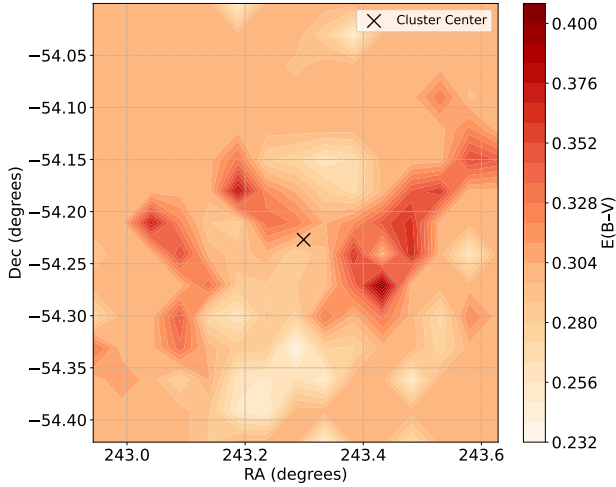

Figure 3. 2D colormap of extinction for the eMSTO stars in NGC 6067 color coded by A_V values taken from A. Khalatyan et al. (2024).

circle in the left panel of Figure 4. Next, we translated the CMD so that the point corresponding to O becomes the origin of the new reference frame. Lastly, we rotated the CMD counterclockwise by an angle θ to align the abscissa with the reddening vector of NGC 6067 to easily estimate reddening differences as shown in the middle panel of Figure 4. The rotation angle θ can be calculated using the following formula:

$$\theta = \arctan\left(\frac{A_G}{E(G_{BP} - G_{RP})}\right).$$

For each MS star in the rotated CMD, we calculated the distance from the fiducial line along the reddening vector,

which gives the residual color ($\Delta x'$) for the particular star. A plot of the y' versus $\Delta x'$ is shown in the right panel of Figure 4. We selected MS stars with G-magnitudes between 14.1 and 16.1 mag as reference stars, as depicted by black points in the left panel of Figure 4. We selected only those stars on the MS in this magnitude range as the reference stars whose distance from the fiducial line was within the 80th percentile to avoid inclusion of the stars with large observational errors or binary companion contamination. For each MS star, we calculated the median of the residual color of the 50 nearest reference stars. This median residual color was taken as the local differential reddening estimate for each star. We then subtracted the median residual color from the residual color of the individual stars to obtain their differential reddening-corrected colors. A comparison between the original MS and the differential reddening-corrected MS in the CMD is shown in Figure 5. While the corrected MS appears slightly narrower, the eMSTO is still present, suggesting that the eMSTO in MS of NGC 6067 is intrinsic and not entirely caused by differential reddening.

4. Spectroscopic Properties of the Stars

We estimated the radial velocity (RV) and the projected rotational velocity, $v\sin i$, of the stars using spectra from the Gaia-ESO archives. The *iSpec* software package was used to derive these velocities (S. Blanco-Cuaresma et al. 2014; S. Blanco-Cuaresma 2019). We used the atomic lines from the Vienna Atomic Line Database provided by F. Kupka et al. (1999) and F. G. Kupka et al. (2000) to estimate the RV values. The velocity profile of the stars for the RV calculation is generated through a cross-match correlation algorithm. The *iSpec* package integrates many atmospheric models and radial
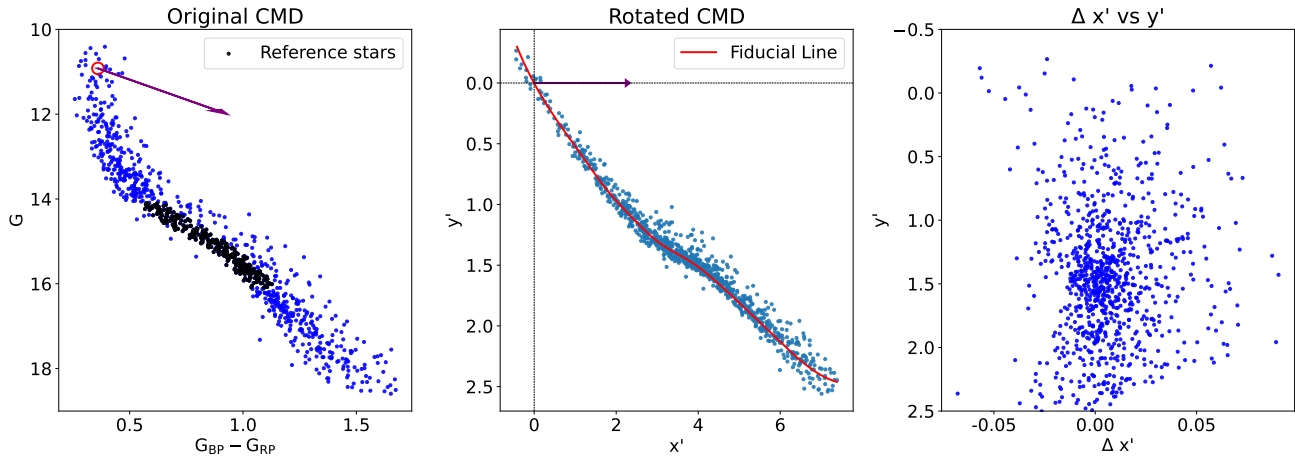
Figure 4. Left panel: observed color–magnitude diagram of NGC 6067 where the reddening vector is shown by an arrow. Middle panel: CMD in the rotated frame, which is considered as a new reference frame for the differential reddening measurements. The red curve represents the fiducial line in the new reference frame. The reddening vector, which becomes parallel to the x'-axis in the new reference frame is shown by an arrow. Right panel: a plot of y' vs. $\Delta x'$ estimated in the new reference frame.

Figure 5. The comparison between original CMD (left panel) and differential reddening corrected CMD (right panel) of the NGC 6067 cluster.

transfer codes together to generate synthetic spectra. The $v\sin i$ values for the stars were estimated by fitting the synthetic spectra on the observed spectra of the stars through the χ^2 minimization process. We used the ATLAS9 atmospheric models with the SPECTRUM radial transfer codes to generate the synthetic spectra (R. O. Gray & C. J. Corbally 1994; R. L. Kurucz 2005). We adopted the reference solar abundances from N. Grevesse et al. (2007). The microturbulence velocity, ξ, for the stars except RGB stars were taken as a fixed value of 2 km s^{-1} (A. Mucciarelli 2011). We took advantage of the high-resolution UVES data available for RGB stars to estimate the ξ values for each of them iteratively, as discussed in Section 4.1. Following the described process, we estimated $v\sin i$ values for 35 out of 41 eMSTO stars possessing spectra, 2 BSS stars, and 14 RGB stars. The $v\sin i$ values for the remaining six eMSTO stars possessing spectra, including two Be stars and four SB2 stars, were estimated using the GIRFIT code (Y. Frémat et al. 2006) as described in Sections 4.3 and 4.4. The obtained $v\sin i$ values with other physical parameters of the eMSTO and RGB stars are given in Tables 2 and 3, respectively.

The eMSTO stars in NGC 6067 have a wide range of $v\sin i$ values from ∼9 to 336 km s^{-1}. The eMSTO stars in NGC 6067

have masses in the range of ∼2.1–5.3 $M_\odot$. The stars with similar masses on the MS should be fast-rotating in the absence of magnetic braking. However, we found the spread in the rotation rates of the eMSTO stars of similar masses. The possible causes for the spread in the rotation rates of the stars, particularly of the eMSTO stars, are discussed in Section 5. From S. Randich et al. (2022) we utilized $v\sin i$ values for 147 lMS stars in NGC 6067, though their data exclude eMSTO and RGB stars of the NGC 6067 cluster. The lMS stars were mostly slow-rotating stars with an average $v\sin i$ value of 103 km s^{-1}.

4.1. Red Giant Stars

We found 14 RGB stars in the cluster NGC 6067. We utilized high-resolution ($R \sim 51,000$) spectra from the UVES spectrograph to estimate the atmospheric parameters ($T_{\rm eff}$, $\log g$, and [Fe/H]), $v\sin i$, and RV of all RGB stars. First, we estimated the RV of the RGB stars using the process discussed earlier. The estimated RV values for the RGB stars are given in Table 3. The mean RV value for the RGB stars, excluding the star with ID 441, is found to be -38.78 ± 0.02 km s^{-1} with a standard deviation of 1.56 km s^{-1}. The star with ID 441 has an RV value of -45.8 ± 0.3, which may be hosting a binary

Table 2
The List of the eMSTO Stars of the Cluster NGC 6067 Whose *v*sin*i* Values Are Estimated in the Present Study

ID	R.A. (J2000) (deg)	Decl. (J2000) (deg)	*v*sin*i* (km s^{-1})	G (mag)	$G_{BP} - G_{RP}$ (mag)	A_V (mag)	Mass ($M_\odot$)
5	243.41907	−54.12207	83 ± 25	14.0237	0.4831	⋯	2.100
21	243.45750	−54.05466	11 ± 2	13.6478	0.569	0.91 ± 0.16	2.376
42	243.34326	−54.02435	167 ± 40	12.6672	0.334	⋯	3.243
158	243.36082	−54.23372	123 ± 7	10.6857	0.4779	1.03 ± 0.30	4.969
185	243.42523	−54.20733	204 ± 34	11.335	0.4093	1.06 ± 0.40	4.525
198	243.44811	−54.17712	221 ± 30	10.9265	0.3936	0.98 ± 0.35	4.826
229	243.19800	−54.36750	22 ± 1	11.6377	0.3183	0.84 ± 0.20	4.257
252	243.21793	−54.31174	267 ± 30	11.643	0.3357	0.87 ± 0.25	4.252
253	243.18717	−54.31861	192 ± 28	10.0726	0.3783	0.84 ± 0.32	5.287
317	243.02956	−54.31861	24 ± 8	12.1752	0.3607	⋯	3.731
355	243.30353	−54.28999	155 ± 15	10.0688	0.3839	0.68 ± 0.34	5.290
358	243.27002	−54.29227	15 ± 11	14.0485	0.5158	⋯	2.083
374	243.22888	−54.27893	247 ± 25	12.157	0.3114	⋯	3.749
377	243.25697	−54.28682	159 ± 39	12.8615	0.3744	0.80 ± 0.17	3.061
396	243.30973	−54.28621	132 ± 5	10.5764	0.3517	0.89 ± 0.24	5.036
402	243.31943	−54.27146	295 ± 26	11.0653	0.3665	0.80 ± 0.26	4.735
403	243.31142	−54.27231	25 ± 5	10.7236	0.3051	⋯	4.950
420	243.31949	−54.25319	172 ± 32	11.1322	0.3337	0.82 ± 0.32	4.682
438	243.31659	−54.24563	298 ± 58	12.4412	0.443	0.86 ± 0.16	3.466
459	243.28276	−54.24951	53 ± 4	10.8629	0.2764	⋯	4.867
558	243.20743	−54.22533	336 ± 71	11.5725	0.4241	0.94 ± 0.28	4.314
584	243.20327	−54.20562	219 ± 31	11.2306	0.3496	0.85 ± 0.31	4.606
594	243.21838	−54.18101	227 ± 14	10.6999	0.364	0.79 ± 0.27	4.962
621	243.36841	−54.21187	184 ± 40	12.2131	0.4196	1.00 ± 0.21	3.692
625	243.33303	−54.20987	300 ± 43	11.7253	0.3888	0.92 ± 0.20	4.174
626	243.32592	−54.21167	197 ± 25	10.9451	0.4137	0.96 ± 0.34	4.815
656	243.30853	−54.19698	237 ± 31	11.2045	0.3993	0.98 ± 0.29	4.627
662	243.28178	−54.18211	206 ± 22	12.0702	0.3715	⋯	3.842
670	243.32523	−54.16780	262 ± 15	10.1941	0.3577	⋯	5.213
702	243.39956	−54.15892	154 ± 24	10.8433	0.3055	0.83 ± 0.36	4.888
723	243.59273	−54.24999	273 ± 39	10.4091	0.3906	0.80 ± 0.28	5.117
741	243.26174	−54.18064	326 ± 20	11.0325	0.4674	1.01 ± 0.35	4.756
767	243.23453	−54.16001	204 ± 10	10.4417	0.3272	0.89 ± 0.31	5.102
779	243.30219	−54.14578	306 ± 24	11.0685	0.289	0.62 ± 0.29	4.760
797	243.26709	−54.07170	9 ± 4	12.7096	0.3697	0.91 ± 0.22	3.202
807	243.35750	−54.33215	13 ± 0	11.3071	0.3499	⋯	4.548
814	243.31616	−54.33117	154 ± 35	10.748	0.2852	0.81 ± 0.29	4.941

Note. The ID, R.A., decl., *v*sin*i*, *G* band magnitude, $G_{BP} - G_{RP}$ color, extinction in *V* band, and mass of the eMSTO stars are given in columns 1, 2, 3, 4, 5, 6, 7, and 8, respectively.

Table 3
The Estimated Physical Parameters of the RGB Stars in the Cluster NGC 6067

ID	R.A. (J2000) (deg)	Decl. (J2000) (deg)	G (mag)	$G_{BP} - G_{RP}$ (mag)	RV (km s^{-1})	T_{eff} (K)	$\log g$ (cm s^{-1})	*v*sin*i* (km s^{-1})	[Fe/H] (dex)
216	243.099030	−54.418671	9.528	1.590	−38.28 ± 0.14	4664.93 ± 105.61	1.89 ± 0.39	13.6 ± 0.5	−0.14 ± 0.08
269	243.064087	−54.322052	9.247	1.740	−39.01 ± 0.05	4539.85 ± 41.44	1.32 ± 0.20	7.9 ± 0.2	−0.14 ± 0.04
286	243.165848	−54.294777	9.416	1.761	−34.25 ± 0.05	4375.65 ± 34.85	1.36 ± 0.20	5.9 ± 0.3	−0.16 ± 0.08
441	243.322479	−54.234898	8.036	1.446	−45.80 ± 0.29	5793.07 ± 131.01	1.59 ± 0.27	19.5 ± 0.7	−0.16 ± 0.09
457	243.269348	−54.240891	8.858	2.095	−40.98 ± 0.06	4135.44 ± 40.72	1.00 ± 0.17	5.4 ± 0.3	−0.29 ± 0.08
497	243.266754	−54.205204	8.395	2.001	−40.46 ± 0.06	4249.77 ± 28.96	1.20 ± 0.30	5.8 ± 0.3	−0.14 ± 0.09
553	243.237076	−54.220432	8.109	1.875	−39.90 ± 0.07	4358.43 ± 36.43	0.84 ± 0.17	10.0 ± 0.2	−0.16 ± 0.04
590	243.197327	−54.183475	9.578	1.693	−39.48 ± 0.09	4757.37 ± 51.52	1.45 ± 0.16	10.2 ± 0.2	−0.09 ± 0.03
602	243.348312	−54.228546	9.426	1.886	−38.19 ± 0.05	4384.25 ± 43.80	1.64 ± 0.19	5.6 ± 0.3	−0.05 ± 0.04
658	243.310654	−54.189079	9.558	1.705	−38.65 ± 0.06	4728.21 ± 63.13	2.04 ± 0.17	6.4 ± 0.2	0.07 ± 0.03
717	243.337814	−54.165199	9.502	1.633	−39.31 ± 0.14	4731.75 ± 51.29	1.84 ± 0.30	12.7 ± 0.4	−0.13 ± 0.05
805	243.352997	−54.334927	9.317	1.730	−37.86 ± 0.06	4443.43 ± 33.71	1.40 ± 0.24	4.7 ± 0.4	−0.15 ± 0.04
895	243.496063	−54.273777	9.302	1.902	−38.71 ± 0.05	4295.28 ± 52.58	1.04 ± 0.16	5.0 ± 0.3	−0.10 ± 0.05
919	243.433304	−54.281773	9.747	1.668	−39.03 ± 0.07	4994.09 ± 42.96	2.24 ± 0.20	7.8 ± 0.2	0.09 ± 0.03

Note. The ID, R.A., decl., *G*, $G_{BP} - G_{RP}$, radial velocity, effective temperature, surface gravity, projected rotational velocity, and [Fe/H] abundance of the RGB stars are given in columns 1, 2, 3, 4, 5, 6, 7, 8, 9, and 10, respectively.
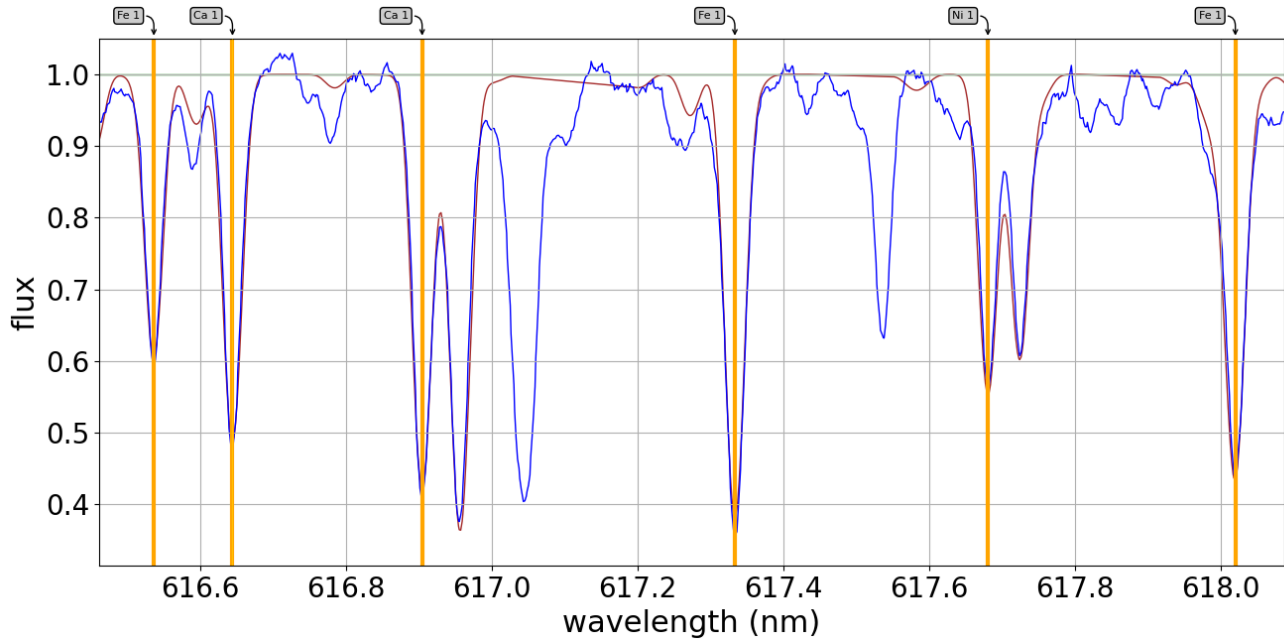
Figure 6. The observed (blue lines) spectrum and best-fit synthetic spectral lines (red lines) for the star with ID 269. The synthetic spectrum was fitted only in segments of 0.1 nm surrounding the selected lines (yellow lines) labeled by corresponding element names on the top of the plot. The best-fit synthetic spectral lines correspond to [Fe/H] $= -0.14 \pm 0.04$ dex.

companion. After RV estimation of the individual stars, we estimated their microturbulence velocity, ξ, while simultaneously varying the T_{eff}, $\log g$, [M/H], $v\sin i$, and ξ. We found mean ξ value as 2.74 ± 0.03 km s^{-1} with a standard deviation of 0.33 km s^{-1}. We then estimated T_{eff}, $\log g$, and $v\sin i$ values for each star by fixing ξ to the obtained values and taking [M/H] as a free parameter. The estimated T_{eff}, $\log g$, and $v\sin i$ values for the RGB stars are given in Table 3.

The slow rotation of the RGB stars makes them suitable candidates to identify the spectral lines corresponding to the elements present. The RGB stars have been useful in determining the [Fe/H] abundances of the open clusters as they are also brighter than the MS stars in an open cluster and exhibit sharper spectral features (A. B. S. Reddy et al. 2013). Therefore, we estimated the [Fe/H] abundances of the RGB stars belonging to NGC 6067. The [Fe/H] abundance of these stars was estimated through the synthetic spectral fitting technique using GES atomic line lists provided by the *iSpec* package. We removed the blended lines from the line list to estimate the metallicity accurately. We also removed the lines that appeared asymmetric from the line list. We fitted synthetic spectral lines on the observed spectra in segments of 0.1 nm around the selected lines while keeping [M/H] and [Fe/H] as free parameters. The spectrum fitting was achieved through the χ^2 minimization technique. The best-fit synthetic spectrum overplotted on the observed spectrum for a star with ID 269 is illustrated in Figure 6. The [Fe/H] values of stars corresponding to the best-fit synthetic spectra are reported in Table 3. The mean [Fe/H] for the RGB stars of NGC 6067 is found to be -0.11 ± 0.02 dex with a standard deviation of 0.09 dex. We considered the mean [Fe/H] value of -0.11 ± 0.02 dex as the [Fe/H] value for the open cluster NGC 6067. The [Fe/H] values of NGC 6067 in the previous studies are very diverse (J. Alonso-Santiago et al. 2017; A. E. Ray et al. 2022). The obtained mean [Fe/H] value reported here is based on a

relatively larger sample of stars with more consistent values for the individual RGB stars.

4.2. Blue Straggler Stars

The BSS are a distinct group of stars that are bluer and brighter than the MS turnoff in the CMD of the star cluster. The stars in an open cluster are considered as coeval populations, there should not be any star bluer than turn-off stars in the upper MS at the location of the BSS. The theories proposed to explain the straggler nature of the BSS stars have mostly one thing in common: the origin of the BSS is related to mass transfer to an MS star. The mass transfer could be from an evolving primary star caused by the Roche-lobe overflow or by collisions between single stars, binary, or triple stellar systems (W. H. McCrea 1964; J. G. Hills & C. A. Day 1976). We detected two BSS stars, which are shown in Figure 2. We estimated $v\sin i$ values for these BSS from the Gaia-ESO spectra as 90 ± 7 and 95 ± 6 km s^{-1}. The relatively fast rotation of the BSS stars in NGC 6067 compared to the general BSS populations seems to support the mechanism of formation through mass transfer in binary systems (F. R. Ferraro et al. 2023; A. C. Nine et al. 2024).

4.3. Be Stars

The nonsupergiant B-type stars with H_{α} emission are known as Be stars (J. M. Porter & T. Rivinius 2003). The Be stars are very rapidly rotating stars hosting dust-free Keplerian disks (T. Rivinius et al. 2013). The fast-rotating properties of the Be stars are useful in confirming the role of stellar rotation in producing the eMSTO in the clusters. We also identified two Be stars with IDs 355 and 626 having H_{β} emission in the upper MS near the turn-off region of NGC 6067. The spectra of these Be stars exhibiting emission features in H_{β} absorption lines are shown in Figure 7.
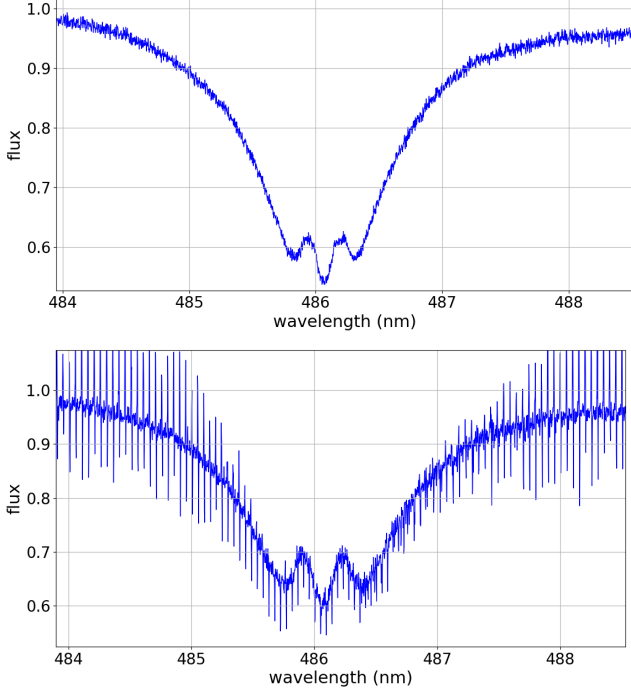
Figure 7. The normalized spectra of the Be stars with IDs 355 and 626 are shown in the upper and lower panels, respectively. The emission features are conspicuous in the H_β (486.1 nm) absorption line of these Be stars.

We estimated the $v\sin i$ values of these Be stars using the GIRFIT code. This code generates model spectra by interpolating in the grids of $T_{\rm eff}$ and $\log g$ values. The model spectra are further convolved to incorporate the rotational and the Gaussian instrumental broadenings. The GIRFIT code utilizes the SYNSPEC (I. Hubeny & T. Lanz 1995) and ATLAS9 (F. Castelli & R. L. Kurucz 2003) models to generate the synthetic spectra. We found $v\sin i$ values to be 155 ± 15 and 197 ± 25 km s^{-1} for the Be stars with IDs 355 and 626, respectively. Furthermore, stars with IDs 402, 403, and 741 are also reported as Be stars by J. Alonso-Santiago et al. (2017), but we lack spectra with a wavelength range containing H_α and H_β for these stars to confirm their Be nature. However, we found large $v\sin i$ values of 295 ± 26 and 326 ± 20 km s^{-1} for stars with IDs 402 and 741, which may be due to their Be nature. The Be stars found in NGC 6067 are occupying the red part of the eMSTO in the CMD, which seems to support the stellar rotation scenario for the origin of the eMSTO in NGC 6067, as Be stars are known to be rapidly rotating stars. The double peak in the emission feature of the H_β line in the Be stars indicates them to belong to the shell stars class of Be stars (See Figure 7). The shape of the emission profile depends on the inclination angle of the line of sight with the disk. The double peak emission feature corresponds to the equator-on view through the excretion disk surrounding the star (T. Rivinius et al. 2006).

4.4. Spectroscopic Binaries

We found four spectroscopic binaries in the eMSTO population of the cluster NGC 6067. These binaries were identified by double peaks in the cross-correlation function (CCF) and spectral line profiles (T. Merle et al. 2017). The star
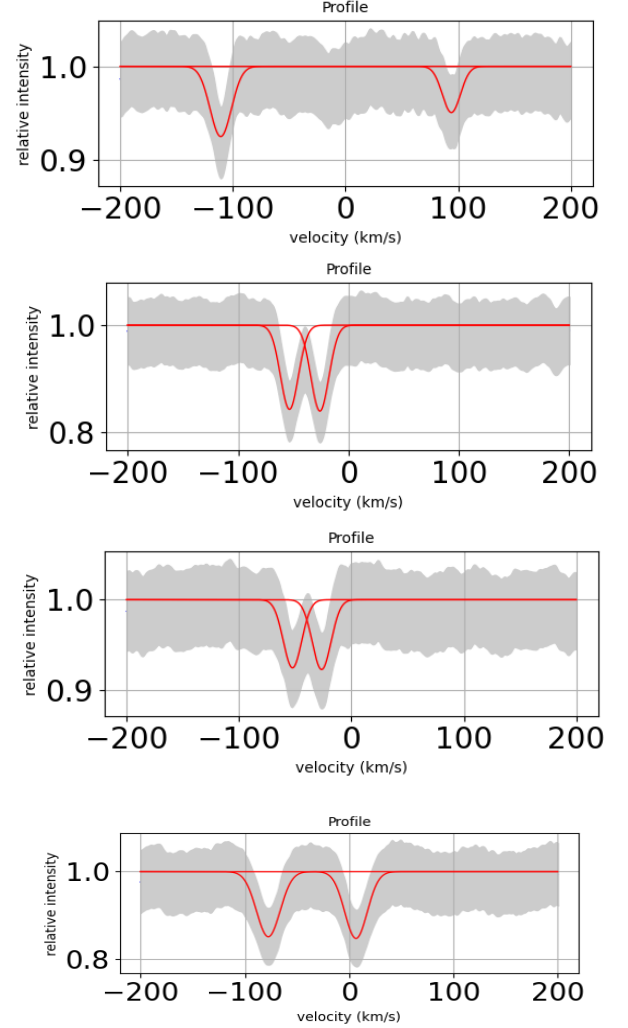

Figure 8. The cross-correlation function of SB2 stars with IDs 70, 609, 643, and 691 found in the eMSTO population of NGC 6067 are shown from top to bottom, respectively.

IDs of these binaries are 70, 609, 643, and 691. These binaries are the SB2, whose spectra contain fluxes from both the primary and secondary binary components. The CCFs of the SB2 binaries are shown in Figure 8.

The CCFs for these SB2 binaries are generated using the *iSpec* package. We estimated $T_{\rm eff}$, $\log g$, $v\sin i$, and RV values of the SB2 stars through a version of the GIRFIT code that takes into account stellar multiplicity (Y. Frémat et al. 2006). The code generates the synthetic spectra for each SB2 component separately and calculates their cross-correlation and corresponding radial velocity. The synthetic spectra are fitted to the observed spectra by minimization of the χ^2, which is achieved through the MINUIT optimization package provided by the CERN. The MINUIT minimization package is based on the Nelder and Meade optimization algorithm. The best-fit spectra of the SB2 stars are illustrated in Figure 9.

Unlike single stars in a cluster, these binary systems display distinct RV values, as their measured RV combine the cluster motion with the orbital velocities of the binary components. The $v\sin i$ values of these binary components are also the lowest among eMSTO stars possibly due to tidal interactions
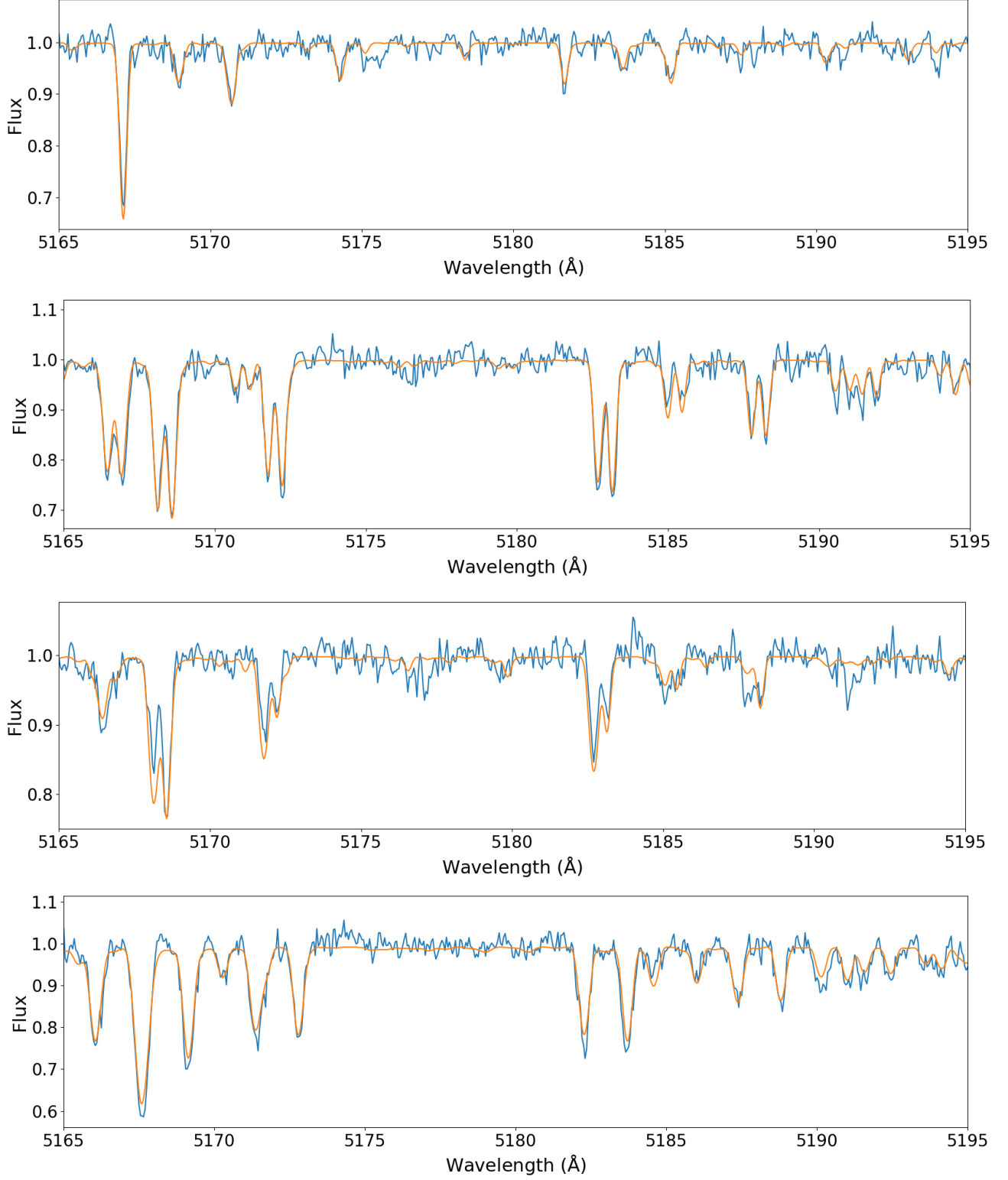
Figure 9. The spectra of the SB2 stars with IDs 70, 609, 643, and 691 are shown by the blue curves (top to bottom), illustrating the best-fit synthetic spectra expressed by yellow curves. The synthetic spectrum fitting for these binary stars is performed by the GIRFIT code.

between binary components. The code is useful in estimating the velocity of the components and the atmospheric parameters of SB2 stars, especially when the components are blended. The estimated T_{eff}, $\log g$, $v\sin i$, and RV parameters of the SB2 components are given in Table 4.

5. Discussion

5.1. Distribution of the $v\sin i$

The open cluster NGC 6067 hosts various types of stars such as Be, SB2, BSS, RGB, and eMSTO stars. The rotational

Figure 10. The color–magnitude diagram of NGC 6067 color coded by the projected rotational velocity of the stars. The black rectangle encloses the eMSTO stars of NGC 6067. The green continuous curve represents the fiducial line for the main-sequence stars.

Table 4
The Physical Parameters of the SB2 Stars Are Estimated Using the GIRFIT Code

	Component A				Component B				
ID	T_{eff}	$\log g$	$v\sin i$	RV	T_{eff}	$\log g$	$v\sin i$	RV	lA/lB
70	13103 ± 89	4.69 ± 0.07	8 ± 0	-110.469 ± 0.127	9123 ± 122	3.92 ± 0.24	8 ± 1	93.023 ± 0.368	0.184 ± 0.016
609	8724 ± 23	3.04 ± 0.05	9 ± 0	-53.315 ± 0.087	8860 ± 22	3.27 ± 0.05	8 ± 0	-25.950 ± 0.072	1.051 ± 0.022
643	10946 ± 46	5.24 ± 0.05	13 ± 0	-52.068 ± 0.164	9585 ± 55	1.81 ± 0.08	8 ± 0	-26.854 ± 0.109	0.633 ± 0.021
691	8412 ± 26	3.30 ± 0.07	14 ± 0	-77.019 ± 0.128	8749 ± 9	3.35 ± 0.06	13 ± 0	5.852 ± 0.128	1.141 ± 0.025

Note. The IDs of the SB2 stars are given in column 1, and the luminosity ratios of the primary and secondary stars are given in column 10. The effective temperature, surface gravity, projected rotational velocity, and radial velocity of the primary components are given in columns 2, 3, 4, and 5, respectively, and those of the secondary components are listed in columns 6, 7, 8, and 9, respectively.

properties of these groups also exhibit very interesting distinctions. The two BSS stars are slow-rotating compared to the eMSTO stars of the cluster, with $v\sin i$ values of 90 ± 7 and 95 ± 6 km s^{-1}. In contrast, the RGB stars are much slower-rotating than the eMSTO stars with $v\sin i$ values below 20 km s^{-1}. Unlike the eMSTO stars, all the RGB stars are slow-rotating stars, as expected, due to the expansion of their envelope and further deepening of the convective envelope causing efficient magnetic braking (A. Sills & M. H. Pinsonneault 2000).

Our main focus of the present study is the eMSTO stars. We found a trend that the stars in the red part of the upper MS are overwhelmingly fast-rotating. Slow-rotating stars are preferentially located in the blue part of the upper MS, as shown in Figure 10.

To further visualize the correlation between $G_{\mathrm{BP}} - G_{\mathrm{RP}}$ color and $v\sin i$ values for the eMSTO stars, we carried out a linear regression fitting to the data points as shown in Figure 11. The pseudo-color $\Delta G_{\mathrm{BP}} - G_{\mathrm{RP}}$ shown on the x-axis of the plot is the color difference of the star with respect to the fiducial line. The fiducial line was created by interpolating the median $G_{\mathrm{BP}} - G_{\mathrm{RP}}$ color and G magnitude of the stars in magnitude bins of 0.5 mag. The points to the left of the fiducial

line were assigned negative $\Delta G_{\mathrm{BP}} - G_{\mathrm{RP}}$ values, whereas those residing right of it were assigned positive values.

The Pearson correlation coefficient for the fitting was found to be 0.506 with p-value = 0.004. We noticed a positive correlation between the pseudo-color $\Delta G_{\mathrm{BP}} - G_{\mathrm{RP}}$ and $v\sin i$ values of eMSTO stars, where redder stars generally rotate faster than their bluer counterparts, as also reported in previous studies (A. F. Marino et al. 2018; W. Sun et al. 2019; S. Kamann et al. 2023). The trend of the preferential location of the fast and slow-rotating stars on the MS continues until $G = 16.3$ mag, starting from the turn-off point. This lower limit of the preferential locations corresponds to the mass of $\sim 1.6\,M_\odot$.

The outliers excluded from the linear regression fitting are shown by red points in Figure 11. The excluded points correspond to eMSTO stars with IDs 21, 229, 317, 358, 403, 797, and 807, which have $v\sin i$ <50 km s^{-1}. A_V values for three stars among these outliers with IDs 21, 229, and 797 are given to be 0.91 ± 0.16, 0.84 ± 0.20, and 0.91 ± 0.22 mag, respectively, by A. Khalatyan et al. (2024). These A_V values are very close to the mean A_V value of 0.93 ± 0.01 for all the eMSTO stars in NGC 6067. Thus, the outlier points for the correlation shown in the figure do not exhibit any significant
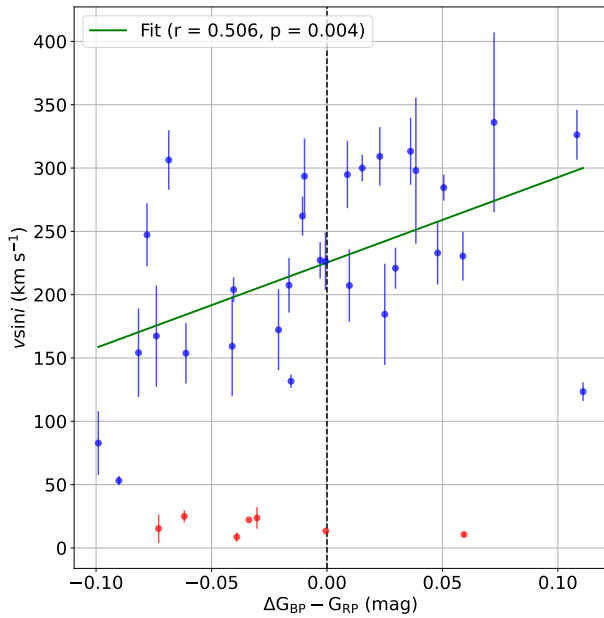
Figure 11. The correlation between pseudo-color $\Delta G_{BP} - G_{RP}$ and $v\sin i$ for the eMSTO stars. The red points show the outliers.

Figure 12. Plot exhibiting fiducial line (shown by the black line) and subgroups of stars in the color–magnitude diagram of NGC 6067. The black asterisks represent outlier stars, as identified in Figure 11.

extinction difference from the remaining eMSTO stars. These excluded slow-rotating stars could be binaries undetectable from the current set of spectroscopic data.

We divided the MS stars into two groups for comparative study of $v\sin i$ distribution in them by drawing a fiducial line as shown in Figure 12.

The bluer eMSTO stars than the fiducial line were grouped as bMS stars, and the redder stars were grouped as rMS stars. There were 146 bMS and 134 rMS stars in the eMSTO region of the cluster NGC 6067. We could estimate the $v\sin i$ values for 23 bMS stars and 18 rMS stars depending on the availability of the spectra of the stars. The bMS stars have an average $v\sin i$ of 146 ± 5 km s^{-1}, which are mostly slow-rotating stars. However, the rMS stars, excluding SB2 stars, are mostly fast-rotating stars having a mean $v\sin i$ value equal to 247 ± 8 km s^{-1}. The spread in the distribution of the rotation rates of stars has also been previously found to be associated with the origin of the eMSTO phenomenon in the star clusters (W. Sun et al. 2019; J. Maurya et al. 2024). However, the mean $v\sin i$ for groups of fast-rotating and slow-rotating stars for star clusters in the previous studies have significantly differed from their obtained values for NGC 6067 (A. F. Marino et al. 2018; S. Kamann et al. 2023; J. Maurya et al. 2024). The average $v\sin i$ value of a star also depends on its mass, as massive stars are expected to rotate faster. Hence, the younger clusters having eMSTO stars more massive than the older clusters are expected to have higher mean $v\sin i$ values for the bMS and rMS stars than older clusters. In our sample of eMSTO stars, we have spectra and thus $v\sin i$ values of generally brighter and more massive stars, which may be a reason for the higher mean $v\sin i$ values for bMS and rMS stars than some previous studies. The metallicity of stars can also influence their rotation rates such that the rotation rates of the stars increase with decreasing metallicity (L. Amard & S. P. Matt 2020; L. Amard et al. 2020). The star clusters in the Magellanic Clouds and the Milky Way have generally different metallicity, which may also cause different mean $v\sin i$ values for bMS and rMS stars.
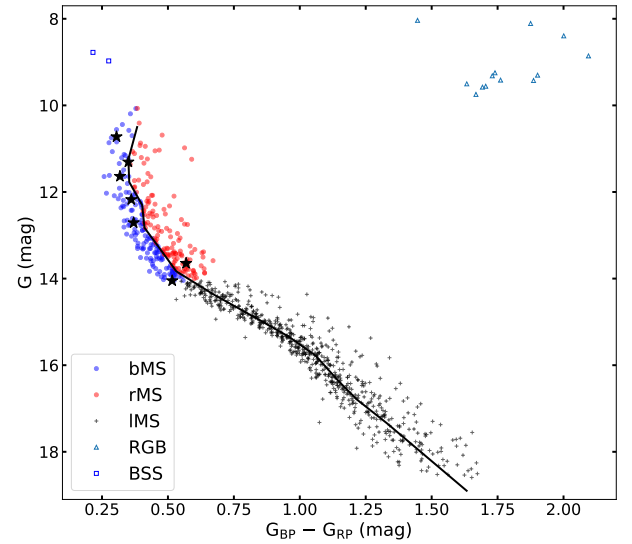
We found two Be stars and four spectroscopic SB2 binaries in the eMSTO population of the cluster NGC 6067. The location of these Be stars is shown in Figure 2. The presence of the Be stars in the red part of the upper MS seems to further support the dependency of the color of the star on its rotational velocity, as the Be stars are known to be fast-rotating stars. The correlation between $v\sin i$ and $G_{BP} - G_{RP}$ color in NGC 6067 could be due to gravity darkening. A few fast-rotating B-type stars may also have a redder color due to the dust-like extinction from their circumstellar excretion disk.

The unresolved binary stars may also broaden the MS as they appear redder than the single stars on the MS. The spectroscopic binary stars are found to be located in the red part of the eMSTO region (see Figure 2). All the spectroscopic binaries detected in the eMSTO population of NGC 6067 comprise slow-rotating components with $v\sin i$ values below 20 km s^{-1}. The slow rotation rates of the binaries might be due to tidal locking. We do not possess enough time-series spectra to efficiently detect the binary stars, especially the low mass-ratio binaries. Therefore, more binary stars might be present in the eMSTO population and we cannot completely rule out the contribution of the photometrically unresolved binaries in broadening the upper MS of NGC 6067.

The fast-rotating stars cease to exist below the mass ~ 1.6 $M_\odot$ in NGC 6067. The lower mass stars are expected to go through magnetic braking due to the strengthening of the magnetic field generated by their convective envelope. The stars go through a transition from the radiative envelope to the convective envelope near the mass of $\sim 1.6\, M_\odot$. The stars with convective envelopes developed stronger magnetic lines, causing the fast loss of angular momentum in the stars, known as the dynamo effect. The absence of the fast-rotating stars in the lower MS of NGC 6067 below $\sim 1.6\, M_\odot$ seems to be caused by magnetic braking.

5.2. Tidal Locking in Binaries

The stars in the upper MS with approximately the same masses are expected to have a similar rotational velocity. However, the conspicuous spread in the distribution of the
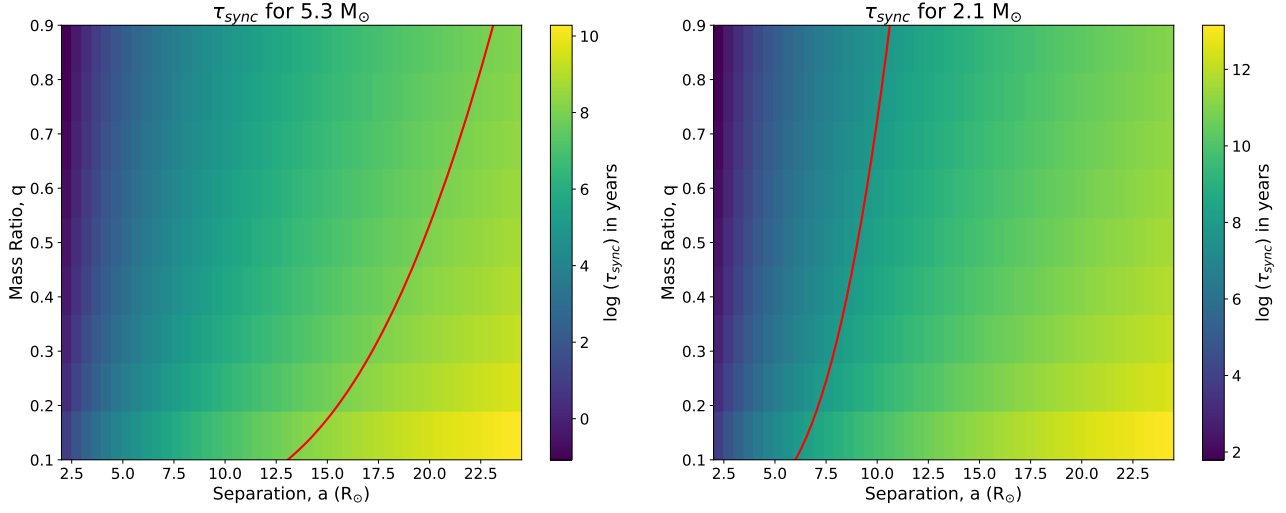
Figure 13. The plot for the correlation between mass ratio, separation, and synchronization time for the binaries to be found in the eMSTO population of the cluster NGC 6067. The colormap represents the synchronization time on a logarithmic scale. The red curve indicates the maximum separation for tidally synchronized binaries relative to the cluster age. The region to the left of the curve corresponds to synchronization times shorter than the cluster age, while the region to the right represents synchronization times longer than the cluster age. The masses corresponding to the synchronization time correlation plots are mentioned at the top of each subplot.

$v\sin i$ values of these stars encourages further exploration of the mechanism responsible for it. It has been suggested that all the stars were initially fast-rotating stars until tidal braking caused some of them to become slow-rotating (F. D'Antona et al. 2015). The initially fast-rotating binary systems change to the effectively tidal-locked binaries as their age reaches the synchronization time for the orbital motion. The synchronization time, $\tau_{\rm sync}$, is the time required for a binary system to synchronize rotational and orbital motions due to tidal locking. We estimated the synchronization time using the following relations provided by J. R. Hurley et al. (2002).

$$\frac{1}{\tau_{\rm sync}} = 5 \times 2^{5/3}\left(\frac{GM}{R^3}\right)^{1/2}\frac{MR^2}{I}q^2(1+q)^{5/6}E_2\left(\frac{R}{a}\right)^{17/2},$$

where G denotes the gravitational constant. a is the separation between primary and secondary. I, M, and R symbolize the moment of inertia, mass, and radius of the primary component, respectively. A brief description for calculating the $\tau_{\rm sync}$ is given in J. Maurya et al. (2024). We calculated the $\tau_{\rm sync}$ values for the masses 2.1 and 5.3 $M_\odot$, representing the lower and upper bounds for the eMSTO stars in NGC 6067. The $\tau_{\rm sync}$ values for binary stars with these masses are shown in Figure 13. Since $\tau_{\rm sync}$ for binary systems negatively correlates with the mass of the primary stars, the $\tau_{\rm sync}$ for any binary present in the eMSTO sample would be between $\tau_{\rm sync}$ values for 5.3 and 2.1 $M_\odot$ stars. We also have marked the maximum possible separation between binary components where $\tau_{\rm sync}$ remains less than or equal to the cluster's age by a red curve in the figure.

Based on the estimated synchronization time, we found that there could be close binaries whose $\tau_{\rm sync}$ would be less than the age of the cluster NGC 6067. Therefore, it is possible that some close binaries in the eMSTO of NGC 6067 would be tidally locked.

The role of the binaries in causing the slow-rotating stars in the blue part of the eMSTO can be assessed by examining the spatial distribution of the stars. If the slow-rotating eMSTO stars were tidally locked binaries then the bMS population, expected to consist predominantly of slow-rotating stars, should be preferentially located in the central region of the cluster due to the mass

segregation effect on these binaries. We calculated the dynamical relaxation time of the open cluster NGC 6067 to investigate the possibility of mass segregation. Dynamical relaxation time is the timescale over which stars in a cluster approach energy equipartition and a Maxwellian velocity distribution through two-body gravitational interactions among member stars. We calculated the dynamical relaxation time, T_E, using the L. Spitzer & M. H. Hart (1971) relation given below:

$$T_E = \frac{8.9 \times 10^5 (Nr_h^3/\bar{m})^{1/2}}{\log(0.4N)},$$

where N denotes the total number of member stars. r_h symbolizes the half mass–radius of the cluster in parsec. The mean mass in solar mass units of the member stars is denoted by $\bar{m}$. The half mass–radius is the radial distance from the cluster center where cumulative mass becomes half of the total mass. The cluster center coordinates (R.A. $= 243\overset{\circ}{.}29517$; decl. $= -54\overset{\circ}{.}23182$) of NGC 6067 were taken from E. L. Hunt & S. Reffert (2024). The masses of individual stars were estimated by fitting P. Marigo et al. (2017) isochrone corresponding to the estimated age of the cluster on the CMD of NGC 6067. We estimated $\bar{m}$ and r_h to be 1.98 $M_\odot$ and 2.85 pc, respectively. We calculated T_E to be 36.2 Myr using estimated $\bar{m}$ and r_h values in the L. Spitzer & M. H. Hart (1971) relation. The estimated T_E value is less than cluster age of 91 Myr, which suggests that the cluster may exhibit mass segregation. We estimated the mass segregation ratio (MSR) using edge length between stars in the minimum spanning tree (MST) method as suggested by R. J. Allison et al. (2009). We used a Python package provided by K. Naidoo (2019) to calculate the MST. The approach used to calculate the MSR is briefly described in J. Maurya et al. (2023). This method is based on the basic principle that massive stars will have shorter mean edge length than that of the low-mass stars in the MST due to segregation. We obtained the MSR to be 1.2 ± 0.1 for NGC 6067. The MSR value very close to unity suggests a weak mass segregation in the cluster. Such a weak mass
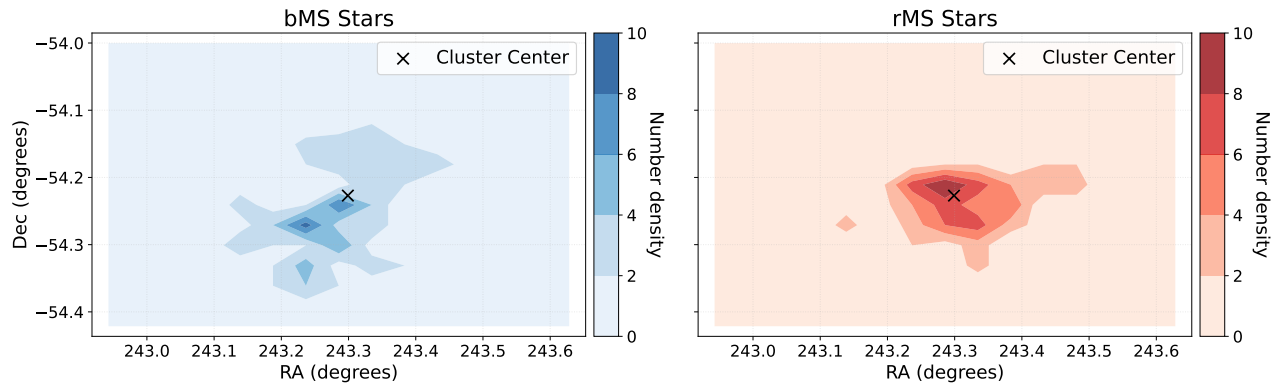
Figure 14. Spatial distributions of the bMS and rMS stars in the form of density contours in NGC 6067. A black cross symbol marks the cluster center in the spatial distribution.

segregation may be due to the fact that the dynamical relaxation process has not yet fully completed. The obtained T_E value of 36.2 Myr, significantly shorter than the cluster's age of 91 Myr, suggests that the cluster has likely reached some degree of dynamical relaxation. However, despite this, we observe only weak mass segregation in the cluster. One potential reason for this weak segregation could be that the dynamical relaxation time we calculated is likely an underestimate. This could be due to the fact that the number of detected member stars in NGC 6067 might be smaller than the true number, owing to the completeness limit of the Gaia-DR3 data. If the total number of member stars were higher, the relaxation time would be longer, implying that the cluster could still be in the process of dynamical evolution, rather than fully relaxed.

The spatial distribution of the eMSTO stars in the form of density contours is shown in Figure 14. For spatial distribution, we created a 15×15 rectangular grid spanning the full range of R.A. and decl. coordinates. The star count in each cell was calculated as the number of stars falling within its boundaries, with empty cells assigned zero counts. We then generated smoothed density contours from these gridded counts to visualize the spatial patterns. The number density shown in the figure is the star count in each cell.

A qualitative inspection of the spatial distribution of the eMSTO stars suggests that rMS stars are more centrally concentrated than bMS stars. This is further quantitatively confirmed by the cumulative radial distribution shown in Figure 15, where rMS stars exhibit a larger normalized cumulative fraction than the bMS stars up to an angular radial distance of 0.̊18. Notably, this angular radial distance is more than twice the core radius of 0.̊08 obtained by E. L. Hunt & S. Reffert (2024) for the cluster NGC 6067. Beyond 0.̊18, the cumulative radial distribution of the bMS population closely follows that of the rMS stars. We tested the hypothesis that the bMS and rMS samples belong to the same radial distribution by performing the Kolmogorov–Smirnov (K-S) test on the samples. The K-S statistic for the bMS and rMS populations was 0.2609 with the p-value = 0.0001. The K-S statistics' obtained value indicates a notable difference in the radial distribution of the two populations. The p-value smaller than 0.05 supports the rejection of the null hypothesis that the two populations follow the same radial distribution.

Although we find evidence of weak mass segregation in the cluster, the bMS population (expected to comprise mostly
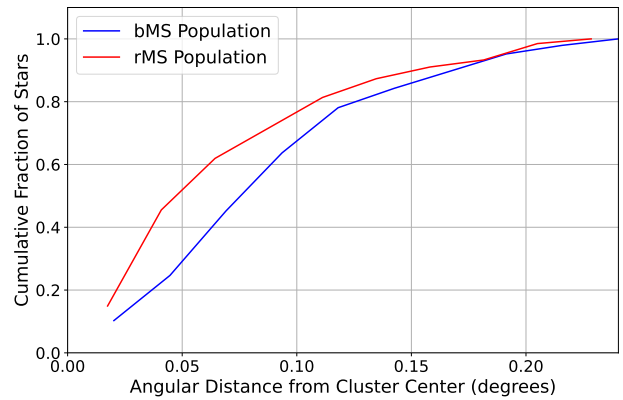

Figure 15. Cumulative radial distributions of the bMS and rMS stars in NGC 6067.

tidally locked binaries) should be preferentially concentrated in the central region of the cluster if there were to be a preferential concentration of any population in the central region at all. The higher concentration of the rMS population, which hosts most of the fast-rotating stars, in the central region of the cluster seems to indicate a factor other than the tidal locking in the binaries contributing to the spread of the rotation rates by slowing down a fraction of the eMSTO stars.

5.3. Environmental Impact on Stellar Rotations

The local environment in the PMS phase influences the rotation rates of the stars (J. Roquette et al. 2021). The environmental influences include the role of far-ultraviolet radiation and dynamical interactions in the evolution and dissipation of the stars' protoplanetary disks. Stars may lose a substantial fraction of their angular momentum through the SDI during the first ∼10 Myr of their lifetime (J. Bouvier et al. 2014). The magnetized stellar winds may extract the angular momentum from the stars through open magnetic field lines, providing spin-down torque balancing the spin-up torque due to accretion on the star (S. Matt & R. E. Pudritz 2005; L. G. Ireland et al. 2021). This spin equilibrium in the accreting star during the SDI phase is simplified as the "disk-locking" process in the theoretical models. The star's rotation rate would be constant due to disk-locking during the lifetime of the disk. The disk-locking prevents the star from spinning up despite its contraction toward the zero-age MS during the PMS phase. After the destruction of the disk, stars become free to spin up while contracting in the PMS phase. Thus, the

environmental influence on the disk dissipation time would also impact the rotational evolution of the stars.

The longer SDI interval would lead to a slower rotation than the shorter SDI time, manifesting in the spread in rotation rates of the eMSTO stars in the cluster (N. Bastian et al. 2020). The SDI mechanism could explain the observed spread in the rotation rates of the eMSTO stars in NGC 6067. The intense radiation from the massive O/B-type stars in the central region of the open cluster causes faster disk dissipation through photoevaporation and, thus, a larger fraction of the fast-rotating stars (L. Venuti et al. 2024). This further explains the preferential concentration of the fast-rotating rMS stars in the central region of NGC 6067 as visible in Figure 14. The outskirts of the cluster NGC 6067 preferentially host slow-rotating bMS stars, possibly due to longer disk dissipation time partly resulting from the lack of massive stars. Additionally, dynamical interactions in the central regions of the cluster can contribute to faster disk dissipation in the PMS phase of the central region stars due to higher density in the cluster center (J. Roquette et al. 2021; L. Venuti et al. 2024).

6. Conclusion

We present a comprehensive analysis of the extended main-sequence turnoff found in the open cluster NGC 6067. We calculate the membership probability of the stars in the NGC 6067 region and obtain a total of 944 member stars, including 280 member stars occupying the eMSTO of the cluster, using the HDBSCAN algorithm to detect the over-density in the proper motion plane. The age of the cluster is found to be 91 Myr through isochrone fitting on the CMD of the cluster. We utilize the medium-resolution spectra from the Gaia-ESO archive available for 41 eMSTO (including four SB2 and two Be), 2 BSS, and 14 RGB stars to estimate the physical parameters of the individual member stars. We study the distribution of the $v\sin i$ for the eMSTO stars and the causes for the obtained distribution. The conclusions from the study can be summarized as follows:

1. The bMS stars are mostly slow-rotating with a mean $v\sin i = 146 \pm 5$ km s^{-1}, whereas predominantly fast-rotating stars in the rMS population have the average $v\sin i = 247 \pm 8$ km s^{-1}. We find a positive correlation between $v\sin i$ and the color of the eMSTO stars, which supports the hypothesis that the eMSTO can originate from the spread in rotation rates of the stars (N. Bastian & S. E. de Mink 2009).

2. We identify two Be stars from their spectra. The Be stars are situated in the right part of the tip of the MS turnoff, which strengthens the spread in the rotation rates scenario for the origin of the eMSTO in NGC 6067, as Be stars are known for their fast rotations.

3. The four SB2 binaries in NGC 6067 occupy the red part of the eMSTO and comprise slow-rotating binary components. The locations of the SB2 binaries suggest that we cannot completely rule out the contribution of the photometrically unresolved binaries in the observed broadening of the upper MS in the CMD of NGC 6067.

4. The synchronization time for the likely close binaries in the eMSTO population suggests that the close binaries in the eMSTO population would be tidally locked if present. However, the spatial distribution and the cumulative radial distribution of the eMSTO stars reveal a higher fraction of the fast-rotating rMS stars compared to the slow-rotating bMS stars in the central region of the cluster. This suggests tidal locking in the binaries to be a less likely mechanism for causing the spread in rotation rates of the eMSTO stars by slowing down a fraction of them.

5. The SDI mechanism suggests that the stars retaining their protoplanetary disks longer tend to be slow rotators, while those with shorter disk lifetimes are typically fast rotators. According to the SDI theory, we would expect to find a higher concentration of fast-rotating stars in the central region of the cluster, as these stars experience more rapid disk dissipation due to photoevaporation and dynamical interactions in the cluster core. The spatial distribution and the cumulative radial distribution of the eMSTO stars seem to support this theory, indicating that the SDI mechanism is most likely responsible for the observed spread in rotation rates and the emergence of the eMSTO in NGC 6067.

ORCID iDs

Jayanand Maurya ● https://orcid.org/0000-0001-5119-8983
Yu Zhang ● https://orcid.org/0000-0001-7134-2874
Sebastian Kamann ● https://orcid.org/0000-0001-6604-0505
Hubiao Niu ● https://orcid.org/0000-0001-5796-8010
Yves Frémat ● https://orcid.org/0000-0002-4645-6017
Kaixiang Lang ● https://orcid.org/0009-0006-1313-4675
Y. C. Joshi ● https://orcid.org/0000-0001-8657-1573
M. R. Samal ● https://orcid.org/0000-0002-9431-6297
Peter De Cat ● https://orcid.org/0000-0001-5419-2042
Ali Esamdin ● https://orcid.org/0000-0003-1845-4900

References

Allison, R. J., Goodwin, S. P., Parker, R. J., et al. 2009, MNRAS, 395, 1449
Alonso-Santiago, J., Frasca, A., Catanzaro, G., et al. 2021, A&A, 656, A149

Alonso-Santiago, J., Negueruela, I., Marco, A., et al. 2017, MNRAS, 469, 1330
Amard, L., & Matt, S. P. 2020, ApJ, 889, 108
Amard, L., Roquette, J., & Matt, S. P. 2020, MNRAS, 499, 3481
Bastian, N., & de Mink, S. E. 2009, MNRAS, 398, L11
Bastian, N., Kamann, S., Amard, L., et al. 2020, MNRAS, 495, 1978
Bastian, N., Kamann, S., Cabrera-Ziri, I., et al. 2018, MNRAS, 480, 3739
Bekki, K., & Mackey, A. D. 2009, MNRAS, 394, 124
Blanco-Cuaresma, S. 2019, MNRAS, 486, 2075
Blanco-Cuaresma, S., Soubiran, C., Heiter, U., & Jofré, P. 2014, A&A, 569, A111
Bouvier, J., Matt, S. P., Mohanty, S., et al. 2014, in Protostars and Planets VI, ed. H. Beuther et al. (Tucson: Univ. Arizona Press)
Cabrera-Ziri, I., Bastian, N., Hilker, M., et al. 2016, MNRAS, 457, 809
Cantat-Gaudin, T., Anders, F., Castro-Ginard, A., et al. 2020, A&A, 640, A1
Cardelli, J. A., Clayton, G. C., & Mathis, J. S. 1989, ApJ, 345, 245
Castelli, F., & Kurucz, R. L. 2003, in IAU Symp. 210, Modeling of Stellar Atmospheres, ed. N. Piskunov, W. W. Weiss, & D. F. Gray (Cambridge: Cambridge Univ. Press), A20
Chen, J., Li, Z., Zhang, S., Deng, Y., & Zhao, W. 2022, MNRAS, 512, 3992
Cordoni, G., Milone, A. P., Marino, A. F., et al. 2023, A&A, 672, A29
D'Antona, F., Dell'Agli, F., Tailo, M., et al. 2023, MNRAS, 521, 4462
D'Antona, F., Di Criscienzo, M., Decressin, T., et al. 2015, MNRAS, 453, 2637
Fabricius, C., Luri, X., Arenou, F., et al. 2021, A&A, 649, A5
Ferraro, F. R., Mucciarelli, A., Lanzoni, B., et al. 2023, NatCo, 14, 2584
Frémat, Y., Neiner, C., Hubert, A. M., et al. 2006, A&A, 451, 1053
Gaia Collaboration, Prusti, T., de Bruijne, J., H., J., et al. 2016, A&A, 595, A1
Gaia Collaboration, Vallenari, A., Brown, A. G. A., et al. 2023, A&A, 674, A1
Georgy, C., Charbonnel, C., Amard, L., et al. 2019, A&A, 622, A66
Goudfrooij, P., Girardi, L., Kozhurina-Platais, V., et al. 2014, ApJ, 797, 35
Gray, R. O., & Corbally, C. J. 1994, AJ, 107, 742
Grevesse, N., Asplund, M., & Sauval, A. J. 2007, SSRv, 130, 105
Groenewegen, M. A. T. 2021, A&A, 654, A20
Hills, J. G., & Day, C. A. 1976, ApL, 17, 87
Hubeny, I., & Lanz, T. 1995, ApJ, 439, 875
Hunt, E. L., & Reffert, S. 2023, A&A, 673, A114
Hunt, E. L., & Reffert, S. 2024, A&A, 686, A42
Hurley, J. R., Tout, C. A., & Pols, O. R. 2002, MNRAS, 329, 897
Ireland, L. G., Zanni, C., Matt, S. P., & Pantolmos, G. 2021, ApJ, 906, 4
Kamann, S., Bastian, N., Gossage, S., et al. 2020, MNRAS, 492, 2177
Kamann, S., Bastian, N., Usher, C., Cabrera-Ziri, I., & Saracino, S. 2021, MNRAS, 508, 2302
Kamann, S., Saracino, S., Bastian, N., et al. 2023, MNRAS, 518, 1505
Khalatyan, A., Anders, F., Chiappini, C., et al. 2024, A&A, 691, A98

Kraft, R. P. 1967, ApJ, 150, 551
Kupka, F., Piskunov, N., Ryabchikova, T. A., Stempels, H. C., & Weiss, W. W. 1999, A&AS, 138, 119
Kupka, F. G., Ryabchikova, T. A., Piskunov, N. E., Stempels, H. C., & Weiss, W. W. 2000, BaltA, 9, 590
Kurucz, R. L. 2005, MSAIS, 8, 14
Lindegren, L., Klioner, S. A., Hernández, J., et al. 2021, A&A, 649, A2
Marigo, P., Girardi, L., Bressan, A., et al. 2017, ApJ, 835, 77
Marino, A. F., Milone, A. P., Casagrande, L., et al. 2018, ApJL, 863, L33
Matt, S., & Pudritz, R. E. 2005, ApJL, 632, L135
Maurya, J., Joshi, Y. C., Samal, M. R., Rawat, V., & Gour, A. S. 2023, JApA, 44, 71
Maurya, J., Samal, M. R., Amard, L., et al. 2024, MNRAS, 532, 1212
McCrea, W. H. 1964, MNRAS, 128, 147
McInnes, L., Healy, J., & Astels, S. 2017, JOSS, 2, 205
Merle, T., Van Eck, S., Jorissen, A., et al. 2017, A&A, 608, A95
Milone, A. P., Bedin, L. R., Piotto, G., & Anderson, J. 2009, A&A, 497, 755
Milone, A. P., Piotto, G., Bedin, L. R., et al. 2012, A&A, 540, A16
Mucciarelli, A. 2011, A&A, 528, A44
Naidoo, K. 2019, JOSS, 4, 1721
Niederhofer, F., Bellini, A., Kozhurina-Platais, V., et al. 2024, A&A, 689, A162
Nine, A. C., Mathieu, R. D., Schuler, S. C., & Milliman, K. E. 2024, ApJ, 970, 187
Palacios, A., Talon, S., Charbonnel, C., & Forestini, M. 2003, A&A, 399, 603
Porter, J. M., & Rivinius, T. 2003, PASP, 115, 1153
Randich, S., Gilmore, G., Magrini, L., et al. 2022, A&A, 666, A121
Ray, A. E., Frinchaboy, P. M., Donor, J., Chojnowski, S. D., & Melendez, M. 2022, AJ, 163, 195
Reddy, A. B. S., Giridhar, S., & Lambert, D. L. 2013, MNRAS, 431, 3338
Riello, M., De Angeli, F., Evans, D. W., et al. 2021, A&A, 649, A3
Rivinius, T., Carciofi, A. C., & Martayan, C. 2013, A&ARv, 21, 69
Rivinius, T., Štefl, S., & Baade, D. 2006, A&A, 459, 137
Roquette, J., Matt, S. P., Winter, A. J., Amard, L., & Stasevic, S. 2021, MNRAS, 508, 3710
Sills, A., & Pinsonneault, M. H. 2000, ApJ, 540, 489
Spitzer, L., Jr., & Hart, M. H. 1971, ApJ, 164, 399
Sun, W., de Grijs, R., Deng, L., & Albrow, M. D. 2021, MNRAS, 502, 4350
Sun, W., Li, C., Deng, L., & de Grijs, R. 2019, ApJ, 883, 182
Turner, D. G. 2016, RMxAA, 52, 223
Venuti, L., Cody, A. M., Beccari, G., et al. 2024, AJ, 167, 120
von Zeipel, H. 1924, MNRAS, 84, 665
Wang, C., Langer, N., Schootemeijer, A., et al. 2022, NatAs, 6, 480